SPARCS-North Wide-field VLBI Survey: exploring the resolved μJy extragalactic radio source population with EVN + e-MERLIN

Ann Njeri [1,2]★ Robert J. Beswick,[1]★ Jack F. Radcliffe [1,3,4]★ A. P. Thomson,[1] N. Wrigley [5]
T. W. B. Muxlow,[1] M. A. Garrett,[1] Roger. P. Deane [2,6] Javier Moldon,[7] Ray P. Norris [8,9]
and Roland Kothes[10]

[1]*Jodrell Bank Centre for Astrophysics, University of Manchester, Oxford Road, Manchester M13 9PL, UK*
[2]*School of Mathematics, Statistics and Physics, Newcastle University, Newcastle upon Tyne NE1 7RU, UK*
[3]*Department of Physics, University of Pretoria, Lynnwood Road, Hatfield, Pretoria 0083, South Africa*
[4]*National Institute for Theoretical and Computational Sciences (NITheCS), 1 Jan Smuts Ave, Braamfontein, Johannesburg 2000, South Africa*
[5]*Jodrell Bank Observatory, Lower Withington, Bomish Ln, Macclesfield SK11 9DW, UK*
[6]*Wits Centre for Astrophysics, School of Physics, University of the Witwatersrand, Private Bag 3, Johannesburg 2050, South Africa*
[7]*Instituto de Astrofísica de Andalucía (IAA, CSIC), Glorieta de las Astronomía, s/n, E-18008 Granada, Spain*
[8]*Western Sydney University, Locked Bag 1797, Penrith South DC, NSW 2751, Australia*
[9]*CSIRO Space and Astronomy, Australia Telescope National Facility, PO Box 76, Epping, NSW 1710, Australia*
[10]*Dominion Radio Astrophysical Observatory, 1 Observatory Crescent, Ottawa, ON K1A 0C6, Canada*

ABSTRACT

The SKA PAthfinder Radio Continuum Surveys (SPARCS) are providing deep-field imaging of the faint (sub-mJy) extragalactic radio source populations through a series of reference surveys. One of the key science goals for SPARCS is to characterize the relative contribution of radio emission associated with active galactic nucleus (AGN) from star formation (SF) in these faint radio source populations, using a combination of high sensitivity and high angular resolution imaging over a range of spatial scales (arcsec to mas). To isolate AGN contribution from SF, we hypothesize that there exists a brightness temperature cut-off point separating pure AGN from SF. We present a multiresolution (10–100 mas) view of the transition between compact AGN and diffuse SF through a deep wide-field EVN + *e*-MERLIN, multiple phase centre survey of the centre of the Northern SPARCS (SLOAN) reference field at 1.6 GHz. This is the first (and only) VLBI (+ *e*-MERLIN) milliarcsecond angular resolution observation of this field, and of the wider SPARCS reference field programme. Using these high spatial resolution (9 pc–0.3 kpc at $z \sim 1.25$) data, 11 milliarcsec-scale sources are detected from a targeted sample of 52 known radio sources from previous observations with the *e*-MERLIN, giving a VLBI detection fraction of ~ 21 per cent. At spatial scales of ~ 9 pc, these sources show little to no jet structure whilst at ~ 0.3 kpc one-sided and two-sided radio jets begin to emerge on the same sources, indicating a possible transition from pure AGN emissions to AGN and SF systems.

Key words: methods: observational – techniques: high angular resolution – techniques: interferometric – galaxies: active – galaxies: high-redshift – quasars: supermassive black holes.

1 INTRODUCTION

The SKA PAthfinder Radio Continuum Surveys (SPARCS)[1] are providing deep-field imaging with multiple SKA pathfinders. These surveys draw upon the unique and complementary qualities of various SKA pathfinder/precursor facilities operating at various resolutions and frequencies, while testing various technical aspects between different instruments (Norris et al. 2013; Norris 2017; Simpson 2017). Using next-generation and upgraded radio telescopes such as the LOFAR, ASKAP, MeerKAT, APERTIF, EVLA, and *e*-MERLIN,

the SPARCS programme is undertaking a series of deep wide-field reference radio continuum surveys to study the formation and evolution of galaxies, cosmological parameters, and the large-scale structures driving them. To utilize these observations, different teams across the globe are developing different techniques such as multiscale deconvolution, source extraction, identification and classification, and multiwavelength cross-identification (e.g. Kondapally et al. 2021; Slijepcevic et al. 2022). These observations, making use of current radio facilities have confirmed that the extragalactic SKA-sky will be dominated by a mixture of intense star-forming galaxies (SFGs), radio-quiet and radio-loud active galactic nucleus (AGN; e.g. Morabito et al. 2017; An et al. 2021; Macfarlane et al. 2021; Whittam et al. 2022). These sources are typically situated between redshifts of 0.5 and 4 with sub-mJy flux densities and in many cases, are luminous

★ E-mail: ann.ngendo@postgrad.manchester.ac.uk (AN);
robert.beswick@manchester.ac.uk (RJB); jack.radcliffe@up.ac.za (JFR)
[1]http://spacs.pbworks.com

merging galaxies often hosting co-evolving star formation (SF) and accretion activity (e.g. Muxlow et al. 2020). Characterizing this radio population with existing observations is vital to guide development of key SKA science programmes, a key scientific objective of the SPARCS programme.

At lower flux densities $S_{1.4\,\text{GHz}} \leq 100\,\mu$Jy, SFGs tend to dominate over faint AGNs. Consequently, there is a requirement to disentangle and distinguish between emissions from AGN accretion and SF (e.g. Padovani 2016; Vernstrom et al. 2016; van der Vlugt et al. 2021). Whilst multiwavelength astronomical approaches such as FIRRC (e.g. Thomson et al. 2014), IRAC colours (e.g. Rawlings et al. 2015), and optical emission line diagnostics (e.g. Law et al. 2021) are making great strides in attempting to characterize these processes, they are not available for every source (e.g. Algera et al. 2020). Furthermore, many of the current radio surveys, including the present SKA pathfinder surveys, are still limited by their angular resolution and are unable to morphologically distinguish all AGN from SFGs. Therefore, a robust method of distinguishing between accretion and SF is essential, independent of the biases associated with multiwavelength classification (e.g. Radcliffe et al. 2021).

High spatial resolution wide-field radio observations provide a key diagnostic for distinguishing between accretion and SF and importantly, spatially resolve and quantify their contributions within individual galaxies (e.g. Morabito et al. 2022). The Very Long Baseline Interferometry (VLBI) distinctly provides high spatial resolution scales, and offers a combination of high point source sensitivity (PSS) and low surface brightness sensitivity which restricts the selection effect to small compact emissions. For example, at $z = 1$, 1 arcsec corresponds to ~ 8 kpc, while 10 mas provided by VLBI corresponds to ~ 8 pc. This unique VLBI characteristic is critical in identifying high brightness temperature ($T_B > 10^5$ K) emissions from compact radio cores and thus constraining emissions from AGNs in these extragalactic radio source populations (e.g. Middelberg et al. 2013; Herrera-Ruiz et al. 2017, 2018; Radcliffe et al. 2018, 2021).

2 VLBI DETECTION RATE VERSUS RESOLUTION

We consider VLBI a clear cut indicator for the presence of accretion activity (Condon et al. 1991; Middelberg & Bach 2008), with current VLBI studies of the high redshift ($z \sim 2$) radio source population having made tremendous strides in isolating AGN contribution from SF at $\sim$ parsec scales (e.g. Chi, Barthel & Garrett 2013; Herrera-Ruiz et al. 2017, 2018; Radcliffe et al. 2018, 2021). However, a gap remains whereby we know little of the radio morphology of these objects at sub-kpc scales and thus the transition point between accretion emission processes associated with compact cores and diffuse/extended emission processes associated with SF remains unclear (e.g. Rees et al. 2016; Hardcastle & Croston 2020). To characterize the true nature of these sources and to isolate AGN contribution from SF, we require intermediate resolution imaging at sub-kpc scales. Since no non-AGN process (except for the very rare radio supernovae) can exceed $T_B > 10^5$ K, we hypothesize that there exists a brightness temperature cut-off point separating pure AGN from SF. To test this hypothesis, we need to achieve and test various angular resolutions between 10 and 200 mas corresponding to various intermediate spatial (sub-kpc) scales at which a radio inteferometric instrument (+ VLBI) becomes sensitive to compact radio emission purely attributed to AGN activity in the host galaxy. This requires optimizing angular resolutions of these VLBI surveys at intermediate spatial scales, with sufficient sensitivity to capture all

AGN contribution and to resolve out all diffuse emissions. This is important if we are to (i) trace the pure spatial extent of SF through cosmic time, and (ii) understand the radio emission mechanisms related to accretion processes in the central core engines which drive the feedback mechanisms in the host galaxy. We also note while a detection at a sufficiently high resolution certainly implies an AGN, the converse is not always true: even a radio-loud AGN does not necessarily yield a VLBI detection, and this is not a function of source strength or sensitivity (Rees et al. 2016).

Combining *e*-MERLIN + VLBI provides a unique prospect of imaging at these intermediate spatial scales. Particularly, combining the EVN + eMERLIN will allow characterization of the μJy radio regime from milliarcsecond scales to $0\overset{''}{.}2$ (~ 10–200 mas). The *e*-MERLIN antennas increase the *uv*-coverage at shorter baselines, thus characterizing the source/jet structure at sub-kpc scales while the EVN longer baselines recover the compact cores at parsec scales. On the other hand, the VLA provides the largest spatial ($>$kpc) scales at $1 - 2$ GHz required for total flux density measurements. Therefore, a combination of these observations with VLBI will provide kpc–parsec imaging spatial scales, essential in probing the most compact radio sources and their accompanying radio jets/structures. This enhanced imaging fidelity will enable the detection of low luminosity radio sources and provide an insight into their morphology. The derived radio spectrum will be useful, for example, in determining whether they are associated with broad absorption lines or thermal radiation for a better understanding of the nature of these radio-quiet objects (e.g. Blundell & Kuncic 2007).

Consequently, we present a wide-field VLBI survey of the SPARCS-North field, by combining (for the first time) the EVN + eMERLIN spatial scales ranging from ~ 10 to 100 mas. This is one of the first multiresolution studies of the faint radio source population at 10–100 mas. Using the multiresolution data and the intermediate spatial scales obtained in this work, we study the transition from compact radio emissions purely associated with AGN to diffuse radio emissions associated with either AGN with jets, SF, or both jets and SF. We detected 11 VLBI sources at 1σ sensitivity of ~ 6 μJy beam^{-1} with ~ 14 h on target. This paper is outlined as follows: we describe the survey design and data reduction strategies in Section 3, including the primary beam corrections for the EVN + *e*-MERLIN array in Section 3.5, and the additional complementary data from the deep wide-field *e*-MERLIN and VLASS radio surveys. In Section 4, we present analysis of radio properties at 10–100 mas multiresolution coverage, which corresponds to 9 pc–0.28 kpc (assuming $z \sim 1.25$) spatial scales. We give a summary of this work and outline the plans for a future further wide-field VLBI survey to increase the source sample and sensitivity in Section 6. Throughout this paper, we adopt the ΛCDM cosmology parameters with $H_0 = 67.4$ km s^{-1} Mpc^{-1} and $\Omega_m = 0.315$ (Planck Collaboration VI 2020) and the spectral index measurements given by the convection $S_\nu \propto \nu^\alpha$, where S_ν is the radio integrated flux density and α is the intrinsic source spectral index.

3 OBSERVATIONS AND DATA REDUCTION

3.1 *e*-MERLIN SPARCS-North

We obtained the SPARCS-North data from the *e*-MERLIN SPARCS Survey carried out on 2018 January 29 at 1.5 GHz for a total of 24 h (P.I. Wrigley). This observations employed a single-pointing strategy centred on RA 15^{h}33^{m}27^s, Dec. 29°12$^{'}$40$^{''}$ covering an area of $\sim$15 arcmin $\times$ 15 arcmin with a restoring beam size of 188 mas $\times$ 170 mas. On-source integration time of $\sim$ 14 h yielded an image with a central
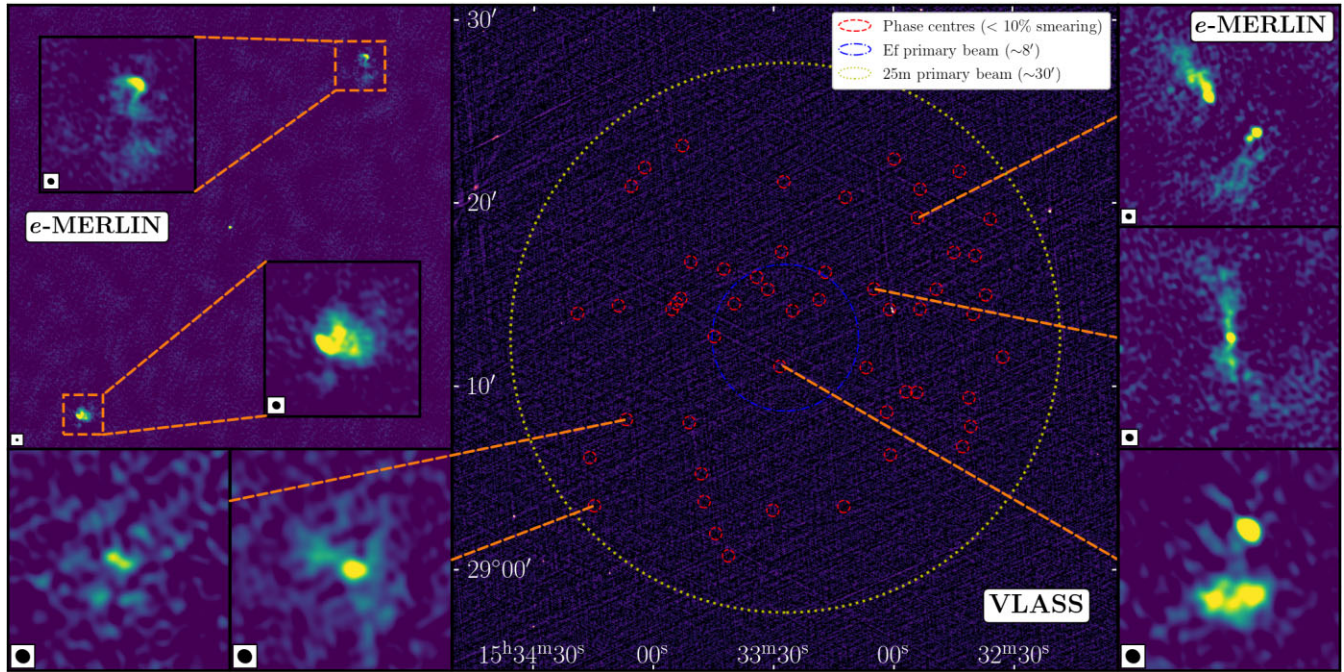
Figure 1. The SPARCS field as seen by the VLASS and *e*-MERLIN surveys. The central plot comprises of the VLASS survey view of this field. Overlaid are the observed phase centres for this survey in the context of the Effelsberg (assuming an effective diameter of 78 m) and the 25 m primary beams of the EVN array. The extent of each phase centre corresponds to 10 per cent half-power beam width (HPBW) smearing, that is, assuming averaging to 2 s integrations and 32 kHz channel width after the initial internal wide-field correlation and a maximum baseline of 10 000 km. Surrounding the VLASS image are postage stamp cut-outs of selected sources from the *e*-MERLIN pilot survey (rms $\sim 10\ \mu$Jy beam^{-1}), revealing the exquisite detail provided by the 0$''$2 high-resolution imaging.

rms sensitivity of $\sim 10\ \mu$Jy beam^{-1}. The 52 phase centres used in our EVN + *e*-MERLIN survey were pre-selected from sources identified in this *e*-MERLIN survey above $\sim 6\sigma$, corresponding to sources with flux densities $> 60\ \mu$Jy (Wrigley et al., in preparation).

3.2 EVN + *e*-MERLIN observations

The SPARCS-North continuum survey with the combined EVN + *e*-MERLIN array was carried out on 2019 November 3 for a total of 19 h with a total on-source integration time of ~ 14 h. Participating EVN antennas are shown in table 1 of Radcliffe et al. (2018). The data were correlated at the Joint Institute for VLBI ERIC (JIVE) in Dwingeloo, the Netherlands. The observation setup frequency was $1594 - 1722$ MHz centred at ~ 1658 MHz, with a total bandwidth of 128 MHz across eight spectral windows and recorded at an aggregate bit rate of 1024 Mbps with an integration time of 2 s. We employed a single pointing observing strategy centred on RA $15^{\rm h}33^{\rm m}27^{\rm s}$, Dec. $29^{\circ}12'40''$ using the multiple phase centre mode of the SFXC correlator (Keimpema et al. 2015). The multiple phase centre strategy was based on the 52 phase centres pre-selected from the *e*-MERLIN SPARCS survey with the furthest phase centre at $\sim 11'\!.6$ from the pointing centre. We aimed to observe all sources detected by *e*-MERLIN ($\geq 60\ \mu$Jy, 6σ), located all over the primary beam of the 25-m antennas (see Fig. 1) in the *e*-MERLIN array. Two sources, J1532+2919 and J1539+2744, were used for phase referencing. The source J1539+2744 (located $\sim 2^{\circ}$ from the target field) was used as the primary phase (and delay) calibrator and was visited once every 30 min. This was further refined by visiting the secondary phase calibrator, J1532+2919 (located 0.27° from the target field) approximately every 7 min. The flux density for the primary calibrator is 198.0 and 42 mJy for the secondary calibrator at

C band (from the Radio Fundamental Catalog, RFC, rfc2019d[2]). The sources 4C39.25 (observed for 6 mins) and J1642+3948 (observed for 6 min and revisited every 4 h) were used as fringe finders.

3.3 VLASS SPARCS-North

We obtained the SPARCS-North images from the NRAO VLA Sky Survey (VLASS) archives. The VLASS is an all-sky Karl Jansky VLA 2–4 GHz survey covering the entire sky visible to the VLA upto a declination of $> -40^{\circ}$ at an angular resolution of $\sim 2''\!.5$ and an expected sensitivity rms of 70 μJybeam^{-1}, across 3 epochs (~ 5500 h) over a cadence of 32 months from 2017 to 2024 September (Lacy et al. 2020). The VLASS covers a total of 33 885deg^2. We used the primary beam corrected image from the first epoch with a sensitivity rms of $\sim 120\ \mu$Jy beam^{-1}.

3.4 Data processing

The data were processed using the CASA based VLBI Pipeline.[3] Before calibration, the raw data were pre-processed by appending the system temperature ($T_{\rm sys}$) measured for each antenna to the FITS-IDI files. The effects of gravity on the shape of the antenna dishes as they move while tracking sources must also be accounted for. These distortions affect the gain of an antenna and are calculated based on the pointing direction of the antenna and the empirically observed properties. Additionally, the observatory flags were translated into CASA flags and finally the VLBI FITS-IDI (AIPS format) files

---

[2] http://astrogeo.org/vlbi/solutions//rfc_2019d
[3] https://github.com/jradcliffe5/VLBI_pipeline

were converted into a measurement set, (MS, CASA format). The observatory flags were then applied to the MS and the correlated visibility amplitudes were scaled to a physically meaningful value using the system temperature measurements (T_{sys}). We also carried out the total electronic content (TEC) correction for the ionosphere-induced dispersive delays. Automated flagging of RFI was conducted using the AOFLAGGER software (Offringa, de Bruyn & Zaroubi 2012) and any remaining bad data were flagged off manually.

The instrumental delays, which show up as jumps in phase between the spectral windows (spws) due to signal delays at each antenna, were removed by solving for the phase and delays on a 1 min integration of the two fringe finders 4C39.25, J1641+3948 and the primary calibrator J1539+2744. The fringe-rates, that is, the derivative of the phase error over time, were set to zero to avoid extrapolating their effects across the entire experiment. The spws were then merged to increase the signal to noise (S/N) and further fringe fitting carried on the primary phase calibrator and the two fringe finders to remove group delays. The solution interval was set to 60 s such that it gave enough S/N to get good solutions, but short enough in order to track the changes in the delays, rates, and phases. After the time-dependent delays were corrected for, the phase and rates were then calibrated and applied to the data. Bandpass calibration was then applied using the task BANDPASS where the two fringe finders and the primary phase calibrator were used.

To correct for the phase errors due to the atmosphere, we used a bootstrapping approach using the primary phase calibrator, J1539+2744 (198 mJy), located at $2°$ from the target field. This was then refined using the fainter (40 mJy) secondary phase calibrator J1532+2919, located closer to the target field at $0.27°$. The primary phase calibrator underwent two rounds of phase only calibration at a solution interval of 60 s and 3 rounds of amplitude and phase calibration. These solutions were then applied to the secondary phase calibrator. The secondary phase calibrator then underwent five rounds of phase only calibration at a solution interval of 60 s. The criterion for phase calibration selection is that the source be located near the target and therefore the solutions derived over time for the phase calibrator are approximately correct for the target source, since the signal path through the atmosphere is similar for both sources. These solutions were then applied to a single phase centre to ensure that the corrections had been applied properly. The flagging tables and the calibration solutions derived for this single subfield were then applied to all the remaining 51 phase centres.

3.5 Primary beam corrections

Heterogenous arrays such as the EVN and *e*-MERLIN have different receptors and different dish diameters which result in each station having a different primary beam response. This manifests as a direction-dependent amplitude error due to differing attenuations of the antenna responses (e.g. Cotton & Mauch 2021; Radcliffe et al., in preparation). We derived corrections for the primary beam response of each antenna in the EVN + *e*-MERLIN array for each of the 52 phase centres based on the primary beam correction equation:

$$P(\theta) = P(0)\exp\left[-\frac{4\ln(2)D_{eff}^2}{\lambda^2}\theta^2\right], \tag{1}$$

where $P(\theta)$ is the corrected primary beam response, $P(0)$ is the normalized primary beam response $= 1$, D_{eff} is the effective dish diameter of the antenna, θ is the positional offset of the source from the pointing centre, and λ is the wavelength of the observation (see table 1 of Radcliffe et al. 2018 for the D_{eff} values adopted).

3.6 Imaging and source extraction

We used WSCLEAN to create 10 arcsec × 10 arcsec images for each of the 52 phase centres. Natural-weighted images were created and five different outer uv-tapers applied. The weights at the highest *uv*-distance were suppressed by a half-Gaussian kernel whose half-width at half-maximum (HWHM) was 1 Mλ, 2 Mλ, 3.5 Mλ, 5 Mλ, and 10 Mλ. with the corresponding resolution at full width at half-maximum (FWHM) ranging from $\sim 11 - 40$ mas as shown in Fig. 2. Taking the weighting function along the *uv*-plane as $W(u, v)$ and sampling by a Gaussian:

$$W(u, v) = \exp\left\{-\frac{(u^2 + v^2)}{t^2}\right\} \tag{2}$$

where t^2 is the tapering parameter (Mλ in this case). Tapering applies smoothing in the image plane by downweighting the long baselines while degrading the angular resolution. This in turn decreases the PSS while increasing the surface brightness sensitivity to extended radio emissions. We applied *uv*-tapering to downweight the contribution from the long baselines and to increase the surface brightness sensitivity on the shorter baselines, particularly along baselines with the Effelsberg and Lovell antennas. We note that the largest antennas requested only contribute to the inner regions of the image, enabling even deeper imaging at a central rms sensitivity ~ 6 μJy beam^{-1}. The non-tapered image gave the highest PSS of 23.0 μJy beam^{-1}, while tapering lowered the PSS. On the other hand, tapering increased the surface brightness sensitivity from 1200 μJy in the non-tapered image to 1660 μJy in the 10Mλ image. The restoring beam sizes, PSS, and the surface brightness across the five tapers are shown in Table 1. The 5 Mλ *uv*-taper produced the optimum PSS and surface brightness sensitivity, beyond which, our observations became too sensitive to diffuse emissions and the point sources remained unresolved as demonstrated in Fig. 2. Therefore, we created two sets of images for each phase centre, a naturally weighted image with no taper applied referred to as the notaper image and the naturally weighted image with a 5Mλ taper applied referred to as the tapered image throughout this paper.

For source extraction, we used the PYBDSF package (Mohan & Rafferty 2015) to determine the peak brightness and flux densities of our VLBI detections. PYBDSF computes basic statistics such as the image parameters, creates background rms and mean images, identifies islands of contiguous source emission whose peak brightness are above a given S/N threshold. The islands are then fitted with multiple Gaussian components in order to minimize the residuals with respect to the background rms, where the Gaussians within a given island are then grouped into discrete sources. We searched for everything above 5σ and filtered the catalogue to our detection thresholds. To eliminate any possibility of having random noise peak brightness exceeding this threshold, we applied the criteria used by Middelberg et al. (2013) to determine true source detections. Briefly, we estimated the number of independent resolution elements, N, based on equation (3) in Hales et al. (2012) combined with equation (6) in Middelberg et al. (2013) which estimates the number of beams exceeding 5σ if the image noise is Gaussian:

$$N_{+5} = N \times \left[1 - \text{erf}\left(5\sqrt{2}\right)\right]/2, \tag{3}$$

We estimated about $\sim 600\,000$ synthesized-beam areas in each $10\rlap{.}''0$ by $10\rlap{.}''0$ image centred on a single-phase centre. The pixel distribution of each image is a Gaussian distribution (Fig. 3) and the probability of misidentifying random noise peak brightness as real detection was high. Assuming that the number of $>5\sigma$ peaks were of order of 10 within the *e*-MERLIN beam area and 5.5σ peaks were
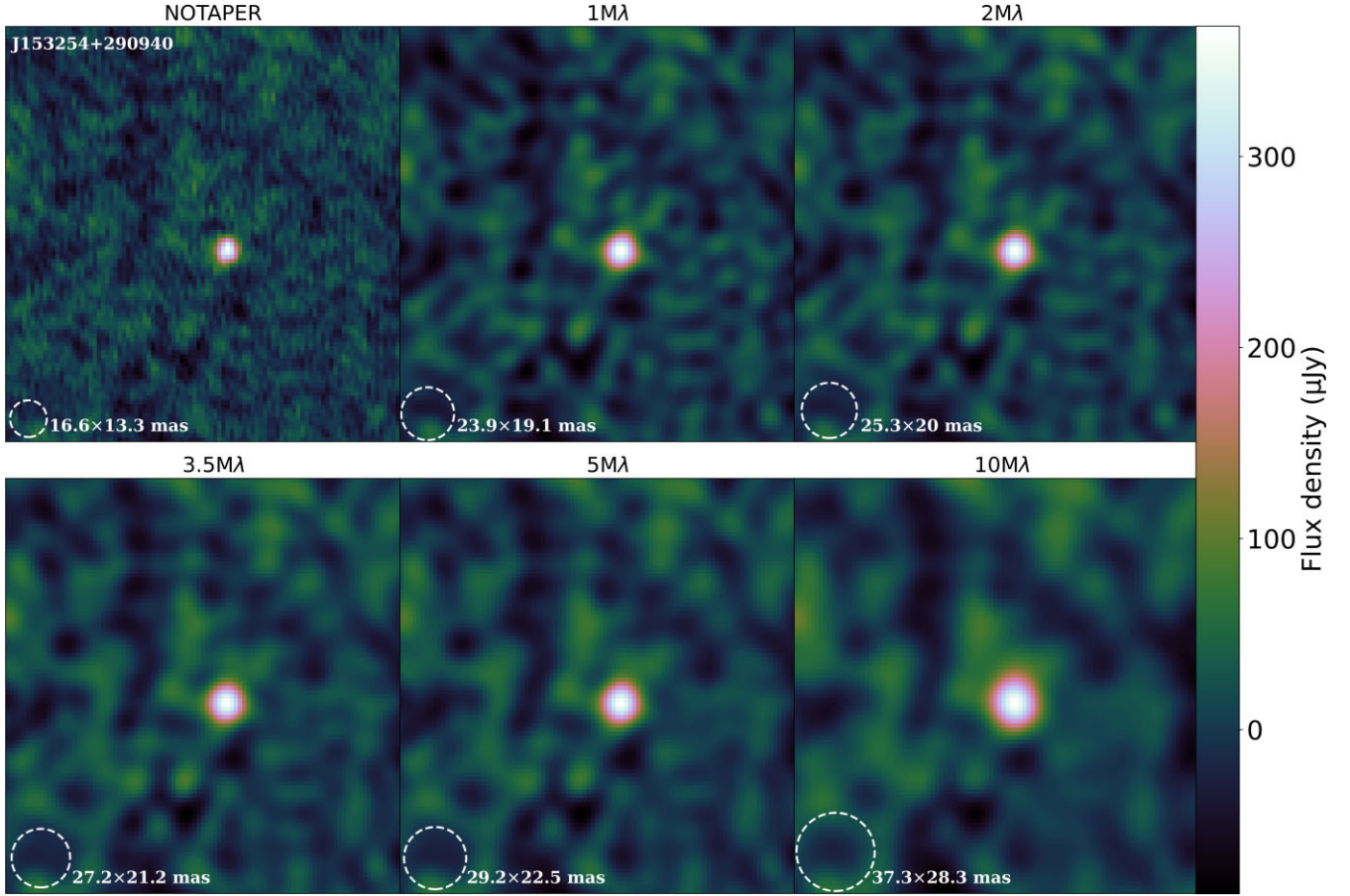
Figure 2. We applied five *uv*-tapers to the natural-weighted image at 1Mλ, 2Mλ, 3.5Mλ, 5Mλ, and 10Mλ which corresponded to an increase in the PSF from $\sim 13 - 40$ mas for the source J153254+290940. The PSS decreased across the imaging at, 23.0 μJy beam^{-1} for the natural-weighted only (NOTAPER) image, 27.9 μJy beam^{-1} across the 1Mλ image, 28.4 μJy beam^{-1} across the 2Mλ image, 29.2 μJy beam^{-1} across the 3.5Mλ image, 30.0 μJy beam^{-1} across the 5Mλ image and 32.4 μJy beam^{-1} across the 10Mλ image. The 5Mλ image corresponded to the optimum detection point for PSS and surface brightness sensitivity and produced the highest peak brightness flux of 387 μJy beam^{-1} across the five *uv*-tapers. Using this optimum taper value of 5Mλ, we produced a set of two images for each of the 52 phase centres, natural-weighted only (notaper image) and natural-weighted with *uv*-tapers applied at 5Mλ (tapered image).

Table 1. Radio properties of the source J153254+290940 at different tapers.

Taper	PSF (mas)	Point source Sensitivity (μJy beam^{-1})	Surface brightness Sensitivity (mJy)
Notaper	16.6 × 13.3	23.0	1.20
1Mλ	23.9 × 19.1	27.9	1.40
1Mλ	25.3 × 20.0	28.4	1.47
2Mλ	27.2 × 21.2	29.2	1.52
3.5Mλ	29.2 × 22.5	30.0	1.60
10Mλ	37.3 × 28.3	32.4	1.66

of order of 100 outside the *e*-MERLIN beam area, we applied the binomial probability distribution function (Middelberg et al. 2013, equation 7) to calculate the true detection rates based on our two search-area criteria:

(i) i) >5.0σ for detections within the *e*-MERLIN beam area of radius ∼ 200 mas, ∼ 0.25 per cent of the total area:

$$B(k = 1|p = 0.0025; n = 10) = \binom{n}{k} p^k (1 - p)^{n-k} = 0.02. \quad (4)$$

(i) ii) >5.5σ for detections outside the *e*-MERLIN beam area within 10 arcsec × 10 arcsec:

$$B(k = 1|p = 0.01; n = 100) = \binom{n}{k} p^k (1 - p)^{n-k} = 0.0003. \quad (5)$$

The number of >5σ noise peaks is smaller <1 across both criteria and further visual inspection ensured our >5σ peaks were coincident with an *e*-MERLIN source. Any >5.5σ peak detection not coincident with an *e*-MERLIN source was unlikely.

4 RESULTS, ANALYSIS, AND DISCUSSION

4.1 No taper imaging

The pixel distribution as a function of sensitivity showed a Gaussian distribution (see Fig. 3) with the highest sensitivity recorded at ∼ 6 μJy beam^{-1}. This sensitivity decreased away from the pointing centre for the 52 phase centres as shown in Fig. 4. The notaper image provided the deepest imaging with a resolution at FWHM of ∼ 17 × 11 mas and a central rms noise of ∼ 6 μJy beam^{-1}. Applying the binomial distribution function equations (4) and (5) as described in Section 3.6, 10 > 5σ VLBI peaks were detected within the *e*-MERLIN beam area of 0″.2 by 0″.2 and 20 > 5.5σ VLBI detections
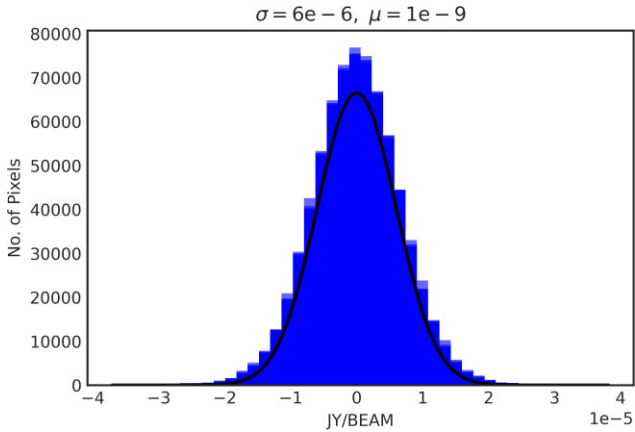
Figure 3. Pixel distribution as a function of sensitivity showing a Gaussian distribution with $\sigma = 6\,\mu\text{Jy beam}^{-1}$ for the notaper image.
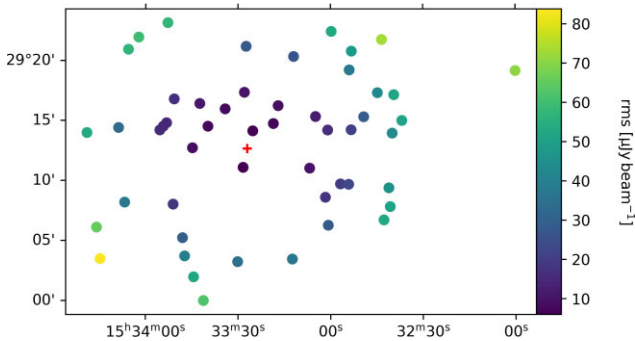
Figure 4. The sensitivity map of the EVN + *e*-MERLIN SPARCS-North survey with a central rms sensitivity of $\sigma \sim 6\,\mu\text{Jy beam}^{-1}$. We computed the rms values of the 52 phase centres from the notaper images. The pointing centre is highlighted by the red cross.

were recorded in the larger $10\rlap{.}''0$ by $10\rlap{.}''0$ area outside of the *e*-MERLIN beam area. We further carried out a visual inspection of these 30 VLBI detections using the *e*-MERLIN image. We confirmed all the 10/10 detections within the *e*-MERLIN beam area as true VLBI detections and 1/20 VLBI detection outside the *e*-MERLIN beam area with a high S/N $>350\sigma$ located at $5\rlap{.}''2$ from the phase centre. In total, we identified 11 VLBI candidates out of the 52 *e*-MERLIN sources. Fig. 5 shows the postage cutouts for these sources at different angular resolutions and sensitivity across the VLASS, *e*-MERLIN, EVN + *e*-MERLIN(notapers), and EVN + *e*-MERLIN(tapered).

4.2 5Mλ tapered imaging

The tapered image optimized both resolution and sensitivity, with a PSF of $\sim 33 \times 21$ mas and a central rms noise of $\sim 7\,\mu\text{Jy beam}^{-1}$. Applying the binomial distribution function equations (4) and (5) as described in Section 3.6, we detected a total of 21 potential VLBI detections, with 7/21 VLBI detections at $>5\sigma$ constrained within the *e*-MERLIN area, and 14/21 5.5σ VLBI detections recorded in the larger $10\rlap{.}''0$ by $10\rlap{.}''0$ image area outside the of *e*-MERLIN beam area. Applying visual inspection of our VLBI detections on the *e*-MERLIN image, we confirmed all the 7/7 > 5σ VLBI detections within the *e*-MERLIN beam area as true detections and 1/14 VLBI detection outside the *e*-MERLIN beam area with a high S/N $>300\sigma$ located at $5\rlap{.}''2$ from the phase centre. In total, we identified eight

VLBI candidates out of the 52 *e*-MERLIN sources. These eight VLBI sources are also detected in the notaper image (see Table 2).

4.3 Astrometry

10/11 sources were detected within a radius of $\sim 0\rlap{.}''2$ of an *e*-MERLIN source in both the notaper and tapered images. The remaining source, J153300+291414, was detected $5\rlap{.}''2$ from the *e*-MERLIN counterpart. The VLBI detections show a median astrometric offset of 23.4 mas in ΔRA and −18.7 mas in ΔDec between this EVN + eMERLIN survey and the *e*-MERLIN survey, shown in Fig. 6.

4.4 Tapered image non-detections

3/11 VLBI detections in the notaper image remained undetected in the tapered image, with 2/3 sources also remaining undetected in VLASS.

We define the flux density ratios, R between the VLBI and *e*-MERLIN as: $R_{\text{notaper}} = S_{\text{i, notaper}}/S_{\text{i, e-MERLIN}}$ for the notaper, and $R_{\text{tapered}} = S_{\text{i, taper}}/S_{\text{i, e-MERLIN}}$ for the tapered image. The R values for the 11 sources are presented in Table 2.

4.4.1 J153419+291359

The source is detected in the notaper image at a 5.5σ but remains undetected in the tapered image due to the increased noise levels. The rms in the tapered image is higher at 73 $\mu\text{Jy beam}^{-1}$ compared to the notaper rms at 53 $\mu\text{Jy beam}^{-1}$. The source has an integrated flux density of $273 \pm 13\,\mu\text{Jy}$ and a peak brightness of $264 \pm 7.4\,\mu\text{Jybeam}^{-1}$ in VLBI and $594.8 \pm 5.7\,\mu\text{Jy}$ and $550.1 \pm 3.1\,\mu\text{Jy beam}^{-1}$ in *e*-MERLIN with $R_{\text{notaper}} = 0.46$. The source remains undetected in VLASS, with the *e*-MERLIN peak brightness $\sim 5\times$ the VLASS rms. If we assume a central frequency of 1600 MHz for the VLBI and the *e*-MERLIN observations and 3 GHz for VLASS we can calculate the ratio depending on the spectral index of the source. Typical extragalactic sources have spectral indices of about -0.77 (e.g. Kellermann 1963), which means that for any source, the VLASS peak should be about 50 per cent of the VLBI peak.

4.4.2 J153406+292056

The source is detected in the notaper image only at 5.2σ. The VLBI integrated flux and peak brightness are $197 \pm 52\,\mu\text{Jy}$ and $307 \pm 29\,\mu\text{Jy beam}^{-1}$ while the *e*-MERLIN integrated flux and peak brightness are $211 \pm 23\,\mu\text{Jy}$ and $301 \pm 16\,\mu\text{Jy beam}^{-1}$ with $R_{\text{notaper}} = 0.9$. The non-detection in the tapered image can be attributed to the fact that this is a very faint source and the noise levels in the tapered image ($\sim 77.5\,\mu\text{Jy beam}^{-1}$) are higher than in the notaper image ($\sim 57\,\mu\text{Jy beam}^{-1}$). The source also remains undetected in the VLASS image, with the *e*-MERLIN peak brightness 2 times the VLASS noise level. This non-detection in VLASS could be attributed to AGN variability (see Section 4.7).

4.4.3 J153354+291431

The source shows binary VLBI compact cores in the notaper image and a single core in the tapered image (see Fig. 8). In the notaper image, the brighter core is detected at S/N ~ 18.4, while the second fainter core is detected at $\sim 5.5\sigma$. In the tapered image, the brighter core is detected at $\sim 14.7\sigma$, while the second fainter core
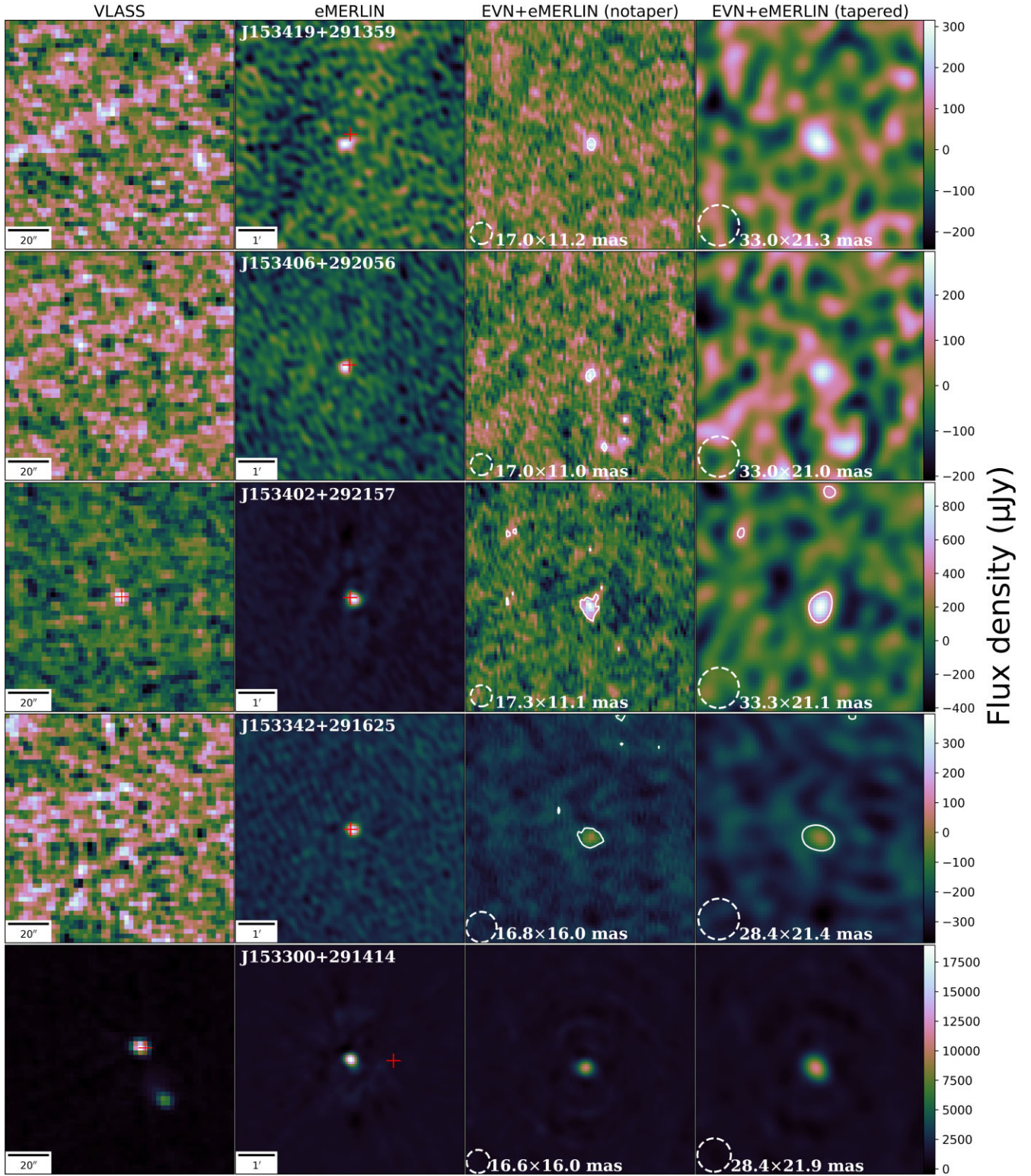
Figure 5. Thumbnails of the SPARCS-North VLBI source sample showing coverage at different angular resolutions and sensitivity across the VLASS (column 1), *e*-MERLIN (column 2), EVN + *e*-MERLIN without tapers (notaper; column 3), and EVN + *e*-MERLIN with tapers (tapered; column 4). The notaper column shows the EVN + eMERLIN natural-weighted image with FWHM ~ 17 × 11 mas, while the tapered column gives the natural-weighted maps tapered at 5Mλ with FWHM ~ 33 × 21 mas. The notaper and tapered cutouts are 40 pixel by 40 pixel on a side. The notaper image offers the highest PSS, sufficient to reveal compact cores within the host galaxies as shown in column 3, while tapering increases the surface brightness sensitivity which reveals the appearance of sub-kpc jet structures around the compact cores, possibly associated with either AGN jets or AGN embedded in star-forming regions as shown in column 4. The red cross indicates the VLBI position in VLASS and *e*-MERLIN. The flux density for the sources across *e*-MERLIN, EVN + *e*-MERLIN (notaper), and EVN + *e*-MERLIN (tapered) can be deduced from the colour bars. The restoring beam size is 2″7 × 2″2 for VLASS and ~0″2 × 0″2 for *e*-MERLIN. Three sources J153419+291359, J153406+292157, and J153342+291625 remain undetected in the VLASS survey.
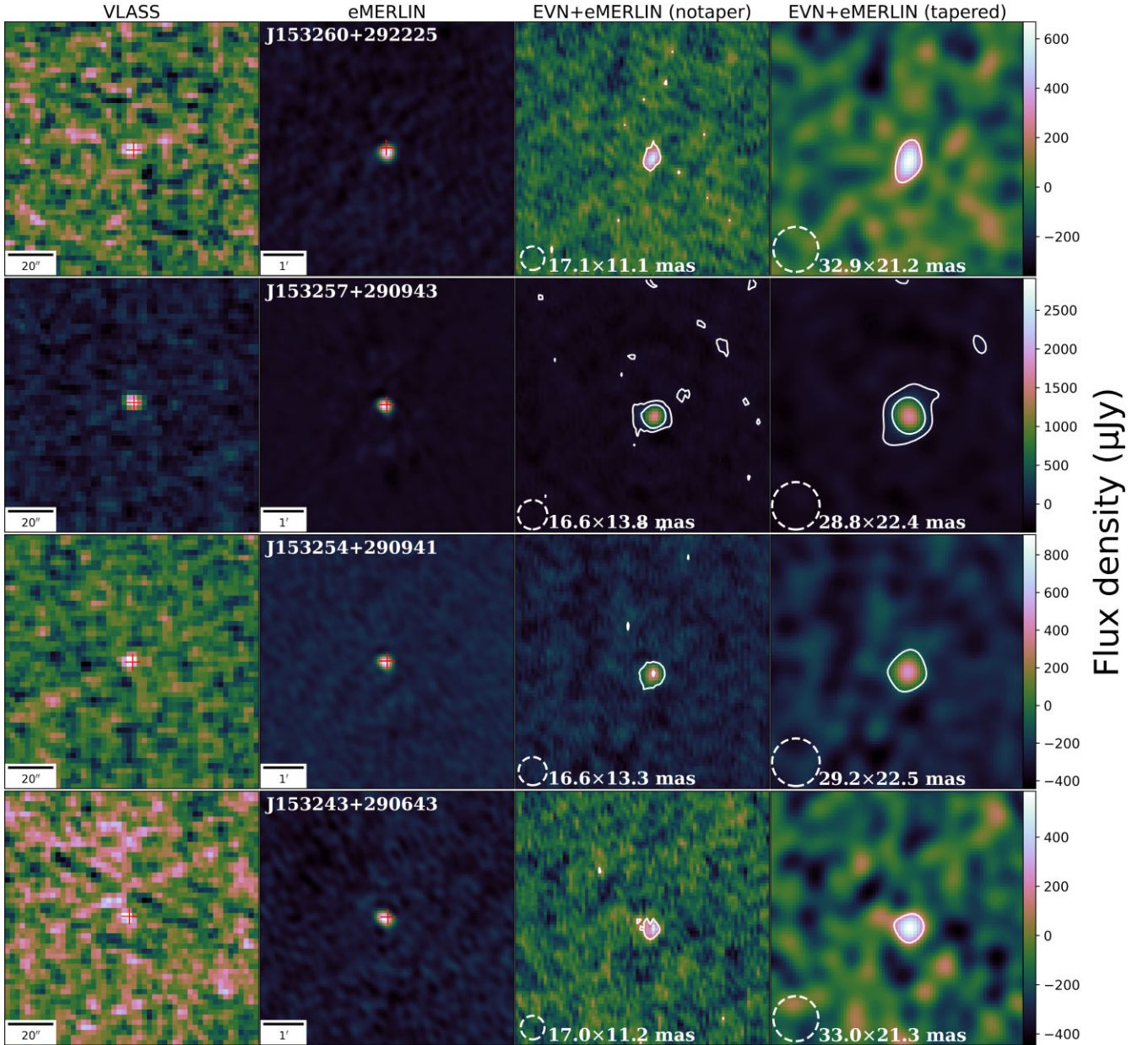
Figure 5. *continued.*

remains undetected. The brightest VLBI core has a flux density of 268.0 ± 17.0 μJy and peak brightness of 282.0 ± 10.0 μJy beam^{-1} in the notaper image with $R_{notaper} = 0.45$, and a flux density of 254.8 ± 6.6 μJy and peak brightness of 278.0 ± 4.0 μJy beam^{-1} in the tapered image with $R_{tapered} = 0.42$. The fainter VLBI core has $R_{notaper} = 0.46$ with a flux density of 74 ± 13 and 75.6 ± 7.4 μJy beam^{-1} in the notaper image. See Section 5 for further analysis and discussion.

4.4.4 J153342+291625

The source has a detection in both the notaper and the tapered images but remains undetected in VLASS. It was detected at S/N 11.1σ in the notaper image and 9.2σ in the tapered image. The notaper VLBI integrated flux density is 117 ± 11 μJy and a peak brightness of 127.1 ± 6.9 μJy beam^{-1} with $R_{notaper} = 0.33$. The integrated flux

and the peak brightness flux across the tapered image are 126 ± 18 μJy and 122.4 μJy beam^{-1}, respectively, with $R_{tapered} = 0.33$. The *e*-MERLIN has a flux density of 352.5 ± 6.4 μJy and a peak brightness flux of 320.4 ± 2.5 μJy beam^{-1} with the *e*-MERLIN peak brightness $\sim 3\times$ the VLASS rms.

4.5 Multiresolution flux density comparison

Excluding the two sources, J153257+290943 and J153300+291414, our VLBI sources have integrated flux and peak brightness ranging from 75 to 665 μJy and 75 to 492 μJy beam^{-1} in the notaper imaging, and 116–465 μJy and 122–629 μJy beam^{-1} across the tapered imaging. The median $R_{notaper} = 0.51$ and $R_{tapered} = 0.55$ implying that we recovered ~ 55 per cent of the *e*-MERLIN flux density across the tapered imaging and ~ 51 per cent across the notaper imaging. The source J153257+290943 has a flux density and peak brightness of

Table 2. Radio properties of the VLBI sources.

Source ID	PC	RA(J2000)	DEC(J2000)	Notaper Beam (mas)	I (μJy)	P (μJy/beam)	S/N	$R_{notaper}$	Beam (mas)	I (μJy)	Tapered P (μJy/beam)	S/N	$R_{tapered}$
J153419+291359	402	15:34:18.9806	+29:13:59.2224	17×15	273±13	264±7.4	5.5	0.46	x	x	x	x	x
J153406+292056	407	15:34:05.5352	+29:20:55.5868	17×11	197±52	307±29	5.2	0.93	x	x	x	x	x
J153402+292157	408	15:34:02.2050	+29:21:56.5011	17×11	573±135	429±55	6.3	0.57	33×21	465±102	629±69	7.3	0.40
J153354+291431	410	15:33:54.1994	+29:14:31.4017	17×15	268±17	282±10	18.4	0.45	28×22	254.8±6.6	278±4	14.7	0.42
J153354+291431	410	15:33:54.1997	+29:14:31.5338	17×11	74±23	75.6±16	5.5	0.46	x	x	x	x	x
J153342+291625	419	15:33:42.3797	+29:16:24.7116	17×16	115±11	127.1±6.9	11.1	0.33	28×21	126±18	117±9.9	9.2	0.36
J153300+291414	435	15:33:00	+29:14:14	–	–	–	>350	–	–	–	–	>300	–
J153260+292225	437	15:32:59.7091	+29:22:24.8132	17×11	511±43	492±24	8.8	0.77	33×21	564±28	570±15	7.8	0.85
J153257+290943	438	15:32:56.7349	+29:09:43.4550	17×14	1328±67	1260±38	64.2	0.55	29×22	1242±35	1280±21	49.4	0.51
J153254+290941	439	15:32:54.0822	+29:09:40.7617	17×13	378±24	369±13	15.7	0.55	29×22	367±10	394.9±6.3	13.0	0.53
J153243+290643	446	15:32:42.6489	+29:06:42.6796	17×11	409±10	360±53	5.9	0.88	33×21	407±38	504±25	6.7	0.87

Note. PC is the source phase centre number. The cross x highlight non-detection in the tapered image. The source PC = 435 showed significant image artefacts around a bright source and thus difficult to deduce the flux density of the source.
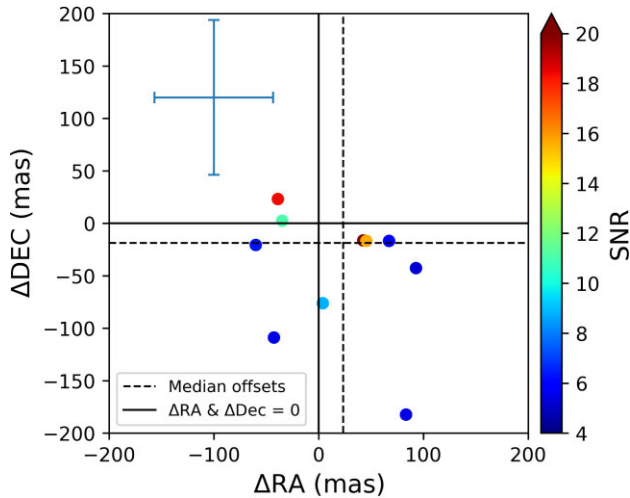
Figure 6. The VLBI astrometric offsets, ΔRA and ΔDec, between the EVN + eMERLIN and the *e*-MERLIN SPARCS-north surveys. The solid black lines indicate ΔRA = 0 and ΔDec = 0 mas while the broken lines indicate the median astrometric offsets 23.4 mas in ΔRA and -18.7 mas in ΔDec. The cross represents the typical error on each source. The VLBI S/N of the sources can be deduced from the colour bar.
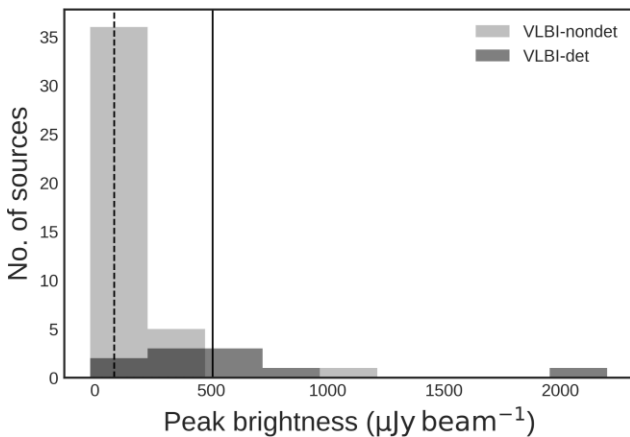
Figure 7. Peak brightness distribution for the 52 *e*-MERLIN sources used as the phase centres in this survey. The region shaded in grey highlights the peak flux distribution for the 41/52 *e*-MERLIN sources that remain undetected (VLBI-nondet) in this survey, while the region highlighted in black shows the peak flux distribution for the 11/52 *e*-MERLIN sources detected (VLBI-det). The vertical lines give the median peak brightness flux, the dotted line is 83.25 μJy beam^{-1} for the non-detections and 506.25 μJy beam^{-1} for the VLBI detections.

1328 μJy and 1260 μJy beam^{-1} in the notaper image and 1242 μJy and 1280 μJy beam^{-1} in the tapered image, while the source J153300+291414 shows some strong artefacts and thus the flux density could not be deduced. Only 3/11 sources are resolved in the notaper image, whereas all sources remained unresolved in the tapered image. This implies that resolutions at FWHM ~ 30 mas, the survey becomes more sensitive to diffuse emissions than compact emissions.

The three VLBI sources, J153419+291359, J153406+292056, and J153354+291431, non-detected in the tapered image have a S/N ~5σ across the notaper imaging. The tapered rms is higher than the notaper rms for all three sources. This implies that the higher PSS achieved in the notaper imaging increases sensitivity

towards very faint compact regions, which are otherwise missed out at intermediate spatial scales. Assuming $z \sim 1.25$, the $11 - 33$ mas recovered in this survey correspond to spatial scales of $\sim 9 - 280$ pc. Furthermore, most of our VLBI sources are point-like and show no jet structure in the notaper image, while all sources show emergence of either one-sided or two-sided jet structures at ~sub-kpc sizes across the tapered image (see Fig. 5). This could indicate that at spatial scales of ~ 0.28 kpc, our survey becomes more sensitive to diffuse emission, associated with either AGN with jets, SF or both, while anything below < 0.28 kpc can be classified as pure AGN. This cut-off spatial scales could potentially pinpoint the transition point from sources dominated by compact emissions purely associated with AGN, to regions dominated by extended diffuse emissions, and thus isolating AGN contribution from SF calculations.

4.6 Compact sources versus extended radio sources

In this VLBI survey, we detected all the 11 compact *e*-MERLIN sources, while the remaining 41/52 non-detected sources showed diffuse and extended radio structures in *e*-MERLIN. This represents a 100 per cent VLBI detection rate for the compact *e*-MERLIN sources. The 41/52 VLBI non-detections have integrated flux densities across the *e*-MERLIN image of ~ 60–2550 μJy with a median of 143.75 μJy, while the 11/52 VLBI detections have 159.10–7500 μJy with a median of 597.10 μJy, respectively. The VLBI non-detections have peak brightness of $6.70 - 1039$ μJy beam^{-1} with a median of 83.25 μJy beam^{-1}, while the 11/52 VLBI detections have peak brightness of $113.40 - 2171$ μJy beam^{-1} with a median of 506.25 μJy beam^{-1}. Fig. 7 shows the peak brightness (μJy beam^{-1}) distribution for the VLBI detected and non-detected sources in the *e*-MERLIN. We expect an *e*-MERLIN source to have a peak brightness $\sim 5 \times$ the local rms (> 300 μJy beam^{-1}) for a detection in VLBI, ~ 82 per cent of the VLBI detections show peak brightness distribution > 300 μJy beam^{-1}. Comparing both the flux density and peak brightness for the VLBI non-detections and VLBI detections and as expected, the VLBI is biased towards very compact cores of the fainter sources with higher peak brightness while the low surface brightness sources remain undetected.

Overall, this represents a VLBI detection rate of ~ 21 per cent at 1σ sensitivity of 6 μJy beam^{-1}. This VLBI detection rate is in agreement with other VLBI detection fractions such as the 20 ± 1 per cent at 1σ sensitivity of 10 μJy beam^{-1} in the VLBA COSMOS survey (Herrera-Ruiz et al. 2017), 20 ± 0.3 per cent at 1σ sensitivity of 60 μJy beam^{-1} in the mJIVE project (Deller & Middelberg 2014), and the 20^{+5}_{-4} per cent at 1σ sensitivity of 55 μJy beam^{-1} in the Chandra deep field south (CDFS) survey.

4.7 AGN variability

3/11 VLBI sources, J153419+291359, J153406+292056, and J153342+291625 remain undetected in VLASS (see Section 4.4). For a VLBI source to be detected in VLASS, we assume that the peak brightness must be $>5\times$ the local rms in VLASS. With a rms sensitivity of ≈ 120 μJy beam^{-1}, the source peak brightness must be > 600 μJy beam^{-1} for a detection in VLASS. All the 8/11 VLBI sources with VLASS counterparts have peak brightness > 600 μJy beam^{-1} in VLASS. Since all 11 VLBI sources are detected in the *e*-MERLIN image, this non-detection in VLASS can be attributed to either variable compact cores or steep spectral indices. Attributing this non-detection to variable compact cores, this could be due to the increase in fluxes as both the VLASS and *e*-MERLIN observations were carried out at different times, with the *e*-MERLIN
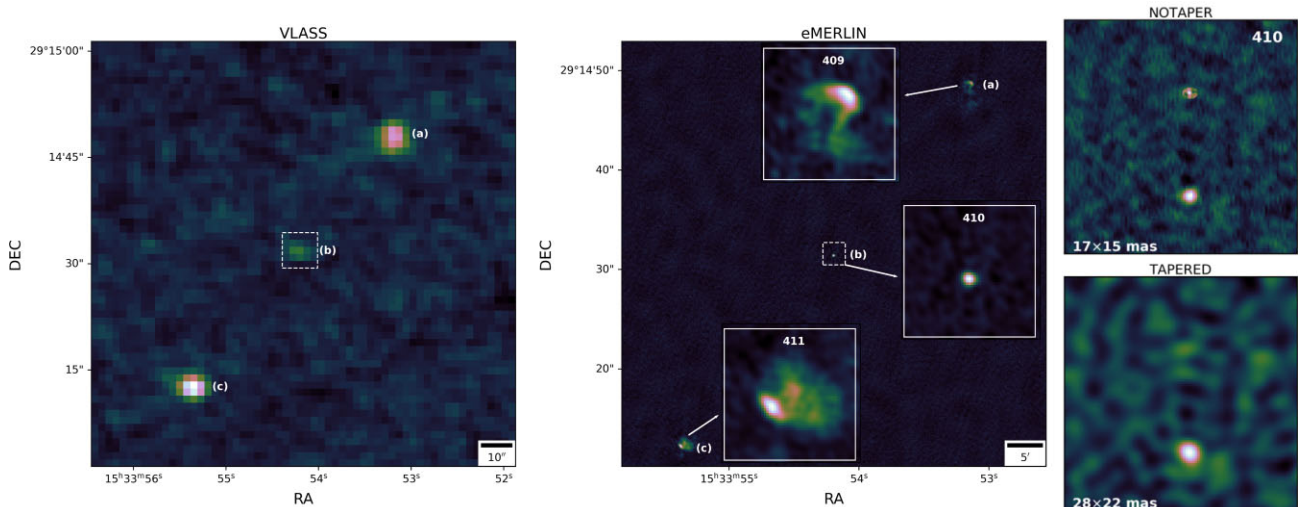
Figure 8. The source J153354+291431 shows two bright compact cores on the VLBI image (NOTAPER and TAPERED), which are located within a double-lobed structure indicating the presence of highly collimated radio jet structures at galactic scales in both the VLASS and the *e*-MERLIN images. The VLASS image shows three unresolved sources at (a), (b), and (c) which correspond to three *e*-MERLIN sources (PC 409, 410, and 411, respectively). Whereas the source at point (b) remains faint and compact in *e*-MERLIN, the sources at points (a) and (c) are resolved out revealing extended radio emissions with edge-brightened outer lobes showing some hot spots. The faint component (b) is coincident with the centre of the host galaxy in both VLASS and *e*-MERLIN. On the other hand, VLBI completely resolves out these outer lobes and hotspots, but only partially resolves the faint component (b) to reveal two bright compact cores in the notaper image. These two VLBI cores are separated by ~ 130 mas corresponding to ~ 1.1 kpc, which is well within the 2.5 kpc orbital separations between paired supermassive black holes proposed by Burke-Spolaor (2011). The fainter (northern core) is detected at $\sim 5.5\sigma$ and the brightest (southern core) is detected at $\sim 18.4\sigma$. In the tapered image, the fainter northern core remains undetected, whereas the brighter southern core is detected at 14.7σ. The distance between the two lobes in *e*-MERLIN is $\sim 46''$, translating to a linear size of ~ 0.4 Mpc, assuming $z \sim 1.25$.

observations taking place ~ 4 months after the VLASS observations. For example, when comparing the first epoch of VLASS (2017–2019) to the FIRST survey (1993–2011), Nyland et al. (2020) show almost a 10-fold flux increase in flux for sources co-located with a known AGN and their results indicate that the slow transient radio sky is dominated by emission mostly attributable to AGN variability, with variability time-scales of a $\sim$ few months. Furthermore, variability studies of the faint μJy radio source population using high radio resolutions and multiwavelength observations have revealed that almost all sources showing variability are AGN (e.g. Radcliffe et al. 2019; Sarbadhicary et al. 2021). ~ 3 per cent of our sources exhibiting potential variability, is in agreement with the short-term variability study of the variable μJy radio sky of Radcliffe et al. (2019) with 3 per cent of their sources exhibiting AGN-related variability. Furthermore, in the CHILES VERDES study of radio variability in the COSMOS field, Sarbadhicary et al. (2021) showed that no star-forming galaxies exhibited any significant variability and therefore attributed all their variability to AGN. From our survey, we further note that a majority (2/3) of these sources potentially exhibiting variability are faint VLBI sources detected at 5.5σ and 5.2σ. At the sensitivity and spatial scales recovered in this survey, we expect to capture pure AGN emissions and therefore, useful in further probing variability as a powerful diagnostic tool for AGN classification. We aim to carry out a similar survey with the *e*-MERLIN and the EVN + *e*-MERLIN probing both short and long-term variability in these radio source populations.

5 SERENDIPITOUS DISCOVERY?

The source J153354+291431 shows two compact VLBI cores in the notaper image and one compact VLBI core in the tapered image that are located within a double-lobed structure in both the VLASS and the *e*-MERLIN images as shown in Fig. 8. The fainter (northern

core) is detected at $\sim 5.5\sigma$ in the notaper image only, while the brightest (southern core) is detected at ~ 18.4 and 14.7σ across both the notaper and tapered images, respectively. The double-lobed structures are well aligned in the north-east and south-west direction across both images, indicating the presence of highly collimated radio jet structures at $\sim$ galactic scales. In the *e*-MERLIN imaging, the double-lobed structure reveal extended radio emissions with edge-brightened lobes showing some hot spots. The two lobes have a separation of ~ 46 arcsec in *e*-MERLIN, translating to a linear size of ~ 0.4 Mpc, assuming $z \sim 1.25$. The unresolved fainter middle component, component (b) in Fig. 8, is coincident with the centre of the host galaxy in both VLASS and *e*-MERLIN. VLBI completely resolves out the outer lobes and partly resolves the fainter middle component to reveal two bright compact VLBI cores separated by a distance of ~ 130 mas (~ 1.1 kpc, assuming $z \sim 1.25$) in the notaper image. This separation distance is well within the 2.5 kpc orbital separations between paired supermassive black holes proposed by Burke-Spolaor (2011) and 1 pc–100 kpc of De Rosa et al. (2019).

The VLASS survey is designed to identify such dual AGN at separations < 7 kpc and binary supermassive black holes within ongoing mergers (Burke-Spolaor et al. 2014, 2018). The VLASS survey detected all the three unresolved components within this system, components (a), (b), and (c) in Fig. 8, which was useful in our host galaxy identification. The *e*-MERLIN observations on the other hand resolve out the extended radio emissions revealing edge-brightened outer lobes with hotspots and are therefore important for probing active radio galaxies in which accretion on to the central SMBH generates relativistic jets resulting in large-scale environments as is the case with this source (e.g. Croston et al. 2019; Hardcastle et al. 2019; Mingo et al. 2019). VLBI observations completely resolve out all the extended emissions associated with the host galaxy, and partly resolves the faint middle component revealing the two compact cores at the centre of this galaxy. This shows that,

even at the smallest orbital separations, mas resolutions provided by VLBI are perfect for exploring and identifying dual AGN or binary SMBHs, particularly within merging galaxy systems which are otherwise difficult to identify as double systems as evidenced here. This amplifies the importance of VLBI in the study of binary systems in post-merger galaxy systems (e.g. Van Wassenhove et al. 2012), stalling in binary black holes in the intermediate stages, besides providing statistical estimates of the rate of SMBH inspiral at various phases (e.g. Burke-Spolaor 2011; Arca-Sedda & Capuzzo-Dolcetta 2019; Mingarelli 2019).

This source is a possible paired SMBH candidate, in a massive (~ 0.4 Mpc in size) radio-loud AGN (RLAGN) system. This possible serendipitous discovery is unique but not entirely unexpected, as shown in similar high-resolution VLBI discoveries. For example, Spingola et al. (2019) found two unexpected gravitational lensing candidates within the wide-field mJIVE-20 survey (Deller & Middelberg 2014). These two candidates can be used to constrain the subhalo mass function which in turn influences the constrains of the cosmological parameters and galaxy formation models (Spingola et al. 2018). Herrera-Ruiz et al. (2017) also finds two unexpected binary SMBH candidates within the VLBA-COSMOS survey. We aim to propose an even deeper follow-up survey to confirm the nature of this source (following e.g. Deane et al. 2014; Breiding et al. 2022) and to further probe phenomena such as merger-induced SBMH growth with simulations predicting a peak in the growth rate at 1–10 kpc (Van Wassenhove et al. 2012) and 0.1–2 kpc (Blecha, Loeb & Narayan 2013).

6 CONCLUSIONS

We have presented a direct view of AGN in the host galaxies and the physical interplay between SF and the nuclear activity through a multiresolution ~ 10–100 mas high dynamic (9 pc–0.3 kpc at $z \sim 1.25$) view of a moderate sample of galaxies. We detect a total of 11 VLBI sources at $>5.0\sigma$ from 52 potential sources based on the *e*-MERLIN survey of the SPARCS-North field. These EVN + *e*-MERLIN data provide the radio flux densities and morphology information required to isolate pure AGN from SF processes within individual galaxies. Despite the small sample size, this information reduces the systematic uncertainties by quantifying the AGN contributions to be subtracted from calculations of SF based on radio continuum. In principle, this survey permits the inclusion of galaxies with AGN hosts which would normally be excluded from such calculations, as evidenced by sources J153419+291359, J153406+292056, and J153354+291431. This is absolutely necessary if we are to obtain the tightest ever constraints on the SF measurements and to resolve out the total contribution of AGN to the cosmic SF history of the host galaxies (e.g. Macfarlane et al. 2021).

At spatial scales of ~ 9 pc, the sources show little to no jet structure whilst at ~ 0.3 kpc one-sided and two-sided radio jets start to emerge on the same sources, indicating a possible transition from pure AGN emissions to AGN plus SF systems. The arcsecond spatial resolutions offered by the *e*-MERLIN and VLA are important in identifying the host galaxies within this faint (μJy) radio source populations, the VLBI on the other hand has a selection bias towards high temperature brightness $> 10^5$ K and therefore sensitive to compact emissions mostly indicative of AGN. This arcsecond-VLBI combination favours systems aligned to the line of sight, thus providing a one-sided jet view. This is expected if the jets were moving at relativistic velocities. However, any entrapment of materials in the nuclear region results in the disruption of the flow of these jets, decelerating the jet plasma which results in the appearance of two-sided jets. The intermediate resolutions offered by this survey on scales of parsecs to a few sub-kpc, offer an insight into this processes where the source plasma is slowed down in the surrounding medium resulting into double-sided jets.

Advances in the wide-field VLBI technique and its application opens up possibilities for new discoveries of important astrophysical objects at mas scales, over wide areas. An increase in the sensitivity of radio surveys and the increasing ability to probe the dynamic radio sky at VLBI $\sim$ mas scales, will directly probe the missing population of dual-AGN and binary SBMHs. The SKA-VLBI will play a crucial role in these probes. The European VLBI Network and *e*-MERLIN are key players in these surveys since the angular resolutions provided by the EVN + *e*-MERLIN array, and the recovered spatial scales, will not be matched until SKA Phase 2 (SKA-VLBI). This EVN + *e*-MERLIN survey of the SPARCS field provides a much needed source classification training set for the near-future deep-wide-field VLBI surveys with instruments such as the MeerKAT and the SKA.

DATA AVAILABILITY

Data underlying this article are publicly available in the EVN Data Archive at JIVE at www.jive.eu/select-experiment and can be accessed with project code EN004. The reduced data will be shared on reasonable request to the corresponding author.

REFERENCES

Algera H. S. B. et al., 2020, ApJ, 903, 139
An F. et al., 2021, MNRAS, 507, 2643
Arca-Sedda M., Capuzzo-Dolcetta R., 2019, MNRAS, 483, 152

Blecha L., Loeb A., Narayan R., 2013, MNRAS, 429, 2594
Blundell K. M., Kuncic Z., 2007, ApJ, 668, L103
Breiding P., Burke-Spolaor S., An T., Bansal K., Mohan P., Taylor G. B., Zhang Y., 2022, ApJ, 933, 143
Burke-Spolaor S., 2011, MNRAS, 410, 2113
Burke-Spolaor S., Brazier A., Chatterjee S., Comerford J., Cordes J., Lazio T. J. W., Liu X., Shen Y., 2014, preprint (arXiv:1402.0548)
Burke-Spolaor S. et al., 2018, preprint (arXiv:1808.04368)
Chi S., Barthel P. D., Garrett M. A., 2013, A&A, 550, A68
Condon J. J., Huang Z. P., Yin Q. F., Thuan T. X., 1991, ApJ, 378, 65
Cotton W. D., Mauch T., 2021, PASP, 133, 104502
Croston J. H. et al., 2019, A&A, 622, A10
De Rosa A. et al., 2019, New Astron. Rev., 86, 101525
Deane R. P. et al., 2014, Nature, 511, 57
Deller A. T., Middelberg E., 2014, AJ, 147, 14
Hales C. A., Murphy T., Curran J. R., Middelberg E., Gaensler B. M., Norris R. P., 2012, MNRAS, 425, 979
Hardcastle M. J., Croston J. H., 2020, New Astron. Rev., 88, 101539
Hardcastle M. J. et al., 2019, A&A, 622, A12
Herrera-Ruiz N. et al., 2017, A&A, 607, A132
Herrera-Ruiz N. et al., 2018, A&A, 616, A128
Keimpema A. et al., 2015, Exp. Astron., 39, 259
Kellermann K. I., 1963, AJ, 68, 539
Kondapally R. et al., 2021, A&A, 648, A3
Lacy M. et al., 2020, PASP, 132, 035001
Law D. R. et al., 2021, ApJ, 915, 35
Macfarlane C. et al., 2021, MNRAS, 506, 5888
Middelberg E., Bach U., 2008, Rep. Prog. Phys., 71, 066901
Middelberg E. et al., 2013, A&A, 551, A97
Mingarelli C. M. F., 2019, Nat. Astron., 3, 8
Mingo B. et al., 2019, MNRAS, 488, 2701
Mohan N., Rafferty D., 2015, Astrophysics Source Code Library, record ascl:1502.007
Morabito L. K. et al., 2017, MNRAS, 469, 1883

Morabito L. K. et al., 2022, MNRAS, 515, 5758
Muxlow T. W. B. et al., 2020, MNRAS, 495, 1188
Norris R. P., 2017, Nat. Astron., 1, 671
Norris R. P. et al., 2013, Publ. Astron. Soc. Aust., 30, e020
Nyland K. et al., 2020, ApJ, 905, 74
Offringa A. R., de Bruyn A. G., Zaroubi S., 2012, MNRAS, 422, 563
Padovani P., 2016, A&AR, 24, 13
Planck Collaboration VI, 2020, A&A, 641, A6
Radcliffe J. F. et al., 2018, A&A, 619, A48
Radcliffe J. F. et al., 2019, A&A, 625, C1
Radcliffe J. F., Barthel P. D., Thomson A. P., Garrett M. A., Beswick R. J., Muxlow T. W. B., 2021, A&A, 649, A27
Rawlings J. I. et al., 2015, MNRAS, 452, 4111
Rees G. A., Norris R. P., Spitler L. R., Herrera-Ruiz N., Middelberg E., 2016, MNRAS, 458, L49
Sarbadhicary S. K. et al., 2021, ApJ, 923, 31
Simpson C., 2017, R. Soc. Open Sci., 4, 170522
Slijepcevic I. V., Scaife A. M. M., Walmsley M., Bowles M., Wong O. I., Shabala S. S., Tang H., 2022, MNRAS, 514, 2599
Spingola C., McKean J. P., Auger M. W., Fassnacht C. D., Koopmans L. V. E., Lagattuta D. J., Vegetti S., 2018, MNRAS, 478, 4816
Spingola C., McKean J. P., Lee M., Deller A., Moldon J., 2019, MNRAS, 483, 2125
Thomson A. P. et al., 2014, MNRAS, 442, 577
van der Vlugt D. et al., 2021, ApJ, 907, 5
Van Wassenhove S., Volonteri M., Mayer L., Dotti M., Bellovary J., Callegari S., 2012, ApJ, 748, L7
Vernstrom T., Scott D., Wall J. V., Condon J. J., Cotton W. D., Perley R. A., 2016, MNRAS, 461, 2879
Whittam I. H. et al., 2022, MNRAS, 516, 245

This paper has been typeset from a TeX/LaTeX file prepared by the author.